ORIGINAL PAPER

Mechanochemically synthesized pyrite and its electrochemical behavior as cathode for lithium batteries

Emiliano N. Primo [1,2] · María V. Bracamonte [1,2] · Guillermina L. Luque [3,4] · Paula G. Bercoff [1,2] · Ezequiel P. M. Leiva [3,4] · Daniel E. Barraco [1,2]

Abstract

This study presents a simple and scalable synthesis of pyrite (FeS_2) starting from S and Fe powders, which involves high-energy ball milling of precursor powders followed by a thermal treatment. The formation of the desired product was confirmed by X-ray diffraction, Raman spectroscopy, thermogravimetric analysis, and X-ray photoelectron spectroscopy. After the synthesis, spherical FeS_2 nanoparticles of ~ 85 nm in size were obtained, with a highly crystalline face-centered cubic structure and no secondary phases. The synthesized material was tested as cathode material for lithium batteries. The cathodes delivered good electrochemical lithium storage properties, such as a reversible capacity as high as 470 mAh g^{-1} even after 120 cycles and a good rate capability. Furthermore, aspects regarding the reaction mechanism and common electrochemical features of Li/FeS_2 batteries are discussed.

Keywords Pyrite · Lithium batteries · Mechanochemical synthesis · Cathode

Introduction

Lithium-ion batteries (LIB) are becoming increasingly popular as portable power sources for electronic devices that have

Emiliano N. Primo and María V. Bracamonte contributed equally to this work.

Electronic supplementary material The online version of this article (https://doi.org/10.1007/s10008-019-04294-6) contains supplementary material, which is available to authorized users.

✉ Emiliano N. Primo
eprimo@famaf.unc.edu.ar

✉ María V. Bracamonte
vbracamonte@famaf.unc.edu.ar

1 Instituto de Física Enrique Gaviola (IFEG), CONICET, Ciudad Universitaria, X5000HUA Córdoba, Argentina

2 Facultad de Matemática, Astronomía, Física y Computación (FaMAF), Universidad Nacional de Córdoba, Ciudad Universitaria, X5000HUA Córdoba, Argentina

3 Instituto de Investigaciones en Físico-Química Córdoba (INFIQC), CONICET, Ciudad Universitaria, X5000HUA Córdoba, Argentina

4 Departamento de Química Teórica y Computacional, Facultad de Ciencias Químicas, Universidad Nacional de Córdoba, Ciudad Universitaria, X5000HUA Córdoba, Argentina

high-power operating requirements. However, the energy density and the capacity of LIB depend on many factors, being one of the most important, the cathode's electrochemical performance [5, 21]. Nowadays, commercial cathodes rely on transition metal-based materials, such as $LiNi_{1/3}Mn_{1/3}Co_{1/3}O_2$, $LiCoO_2$, and $LiFePO_4$ [27]. These materials have low specific capacities (around 200 mAh g^{-1}) [27, 48]; therefore, the need to find new active compounds that improve the performance of the cell. This goal can be achieved with materials that work at higher voltages or with those involving multi-electron reactions. Considering this latter aspect, several transition metal sulfides have been studied as cathodes for LIB [12]. In particular, iron (II) sulfide, also known as pyrite, has been acknowledged as a promising cathode material due to its natural abundance, low cost, and non-toxicity [30]. FeS_2 comprises 53.3 wt% of sulfur and 46.6 wt% of iron, organized in a cubic structure. Fe^{2+} cations in pyrite are in a low spin d^6 configuration, making it a diamagnetic and semiconductor material [11, 28]. Regarding its application in lithium batteries, Li/FeS_2 primary battery has been recently launched by Energizer®, which outputs a better performance when compared to the alkaline ones [55]. The discharge of FeS_2 involves four electrons and yields a theoretical specific capacity of 894 mAh g^{-1} [33, 42, 50, 52]. Its use in rechargeable LIB is limited by its poor stability and cycling

at room temperature due to the following: (i) the volume change during lithiation, which causes pulverization of the electrode, (ii) lack of consensus regarding its reversible lithiation/delithiation mechanism which prevents the design of proper electrochemical operation conditions, and (iii) the low ionic and electrical conductivity of the lithiation products.

Synthesis strategies for obtaining FeS_2 are another topic of interest in recent publications of pyrite-based cathodes. Son et al. [32], for example, proposed the synthesis of FeS_2-polyacrylonitrile (PAN) composite using dimethylformamide (DMF) as solvent and a thermal treatment based on a two-step process at 200 °C and 500 °C. The cathodes prepared with FeS_2-PAN showed specific capacities of ~ 500 mAh g^{-1} after 50 cycles, highlighting the importance of the protective PAN layer on the reversibility of FeS_2. Similar results were obtained by Xu et al. [48], who proposed the synthesis of FeS_2 nanocrystals in hierarchical porous carbon using dodecyl amine, ethanol, chloride acid, tetra ethyl orthosilicate, and iron chloride as precursors, among others. The obtained material presented a specific capacity of 720 mAh g^{-1} after 100 cycles. As seen in previous reports, the combination of FeS_2 with other materials can improve the whole electrochemical performance of the battery, but the high cost, toxicity, and complexity of the synthetic routes make these methods not applicable for industrial purposes.

Another alternative to enhance the cyclability of FeS_2 batteries is based on the micro- and nano-structuration of the active material. Recently, Ma and co-workers developed a cathode based on a micro/nano-structured FeS_2 with specific capacities of 216.8 mAh g^{-1} after 730 cycles [24]. Liu et al. [23] prepared pyrite nanocubes with particle sizes of around 80–120 nm via a solvothermal method. They studied the dependence of the formed products with the reaction time between the iron (II) chloride and sulfur precursors. Eighteen hours at 180 °C were necessary to obtain the desired nanocubes, which delivered a reversible discharge capacity of 540 mAh g^{-1} after 50 cycles. The authors related the enhanced lithium storage properties with the higher specific surface area of FeS_2 nanocubes, which can provide more reaction sites to Li$^+$, leading to less polarization. Li et al. [20] proposed the use of pyrite nanowires synthesized by thermal sulfidation of $FeF_3 \cdot 3H_2O$. This method requires a flow oven with two regions of controllable temperature, both higher than 400 °C. Even though the cathodes prepared with FeS_2 nanowires retain a discharge capacity of 350 mAh g^{-1} after 50 cycles at a rate of 0.1 C, the expensive production method makes this strategy complex for large scale applications. Similar drawbacks are found in other publications such as the one of Hu et al. [16], who synthesized FeS_2 microspheres by a solvothermal method using iron sulfate with DMF and ethylene glycol as precursors. The thermal treatment was carried at 180 °C for 8 h. By using this method, the authors achieved capacities of 556 mAh g^{-1} after 50 cycles with

85% of retention capacity. It should be mentioned that there is proof of some toxicity of DMF on animals, plants, and humans after chronical exposition [19]. For this reason, there is a trend to replace this solvent with "greener" ones.

In view of the need of finding not only an eco-friendly, low cost, and simple synthetic route for the production of FeS_2, but also achieving the nano-structuration of the material, we propose here a scalable method to obtain FeS_2 nanoparticles by high-energy ball milling of Fe and S powder precursors. The milling of the powders was done in an inert atmosphere for 72 h, after which they were thermally treated. Our synthesis allowed obtaining highly crystalline pyrite nanoparticles of ~ 85 nm mean particle size and crystallite size of 18 nm, with no secondary phases. The characterization by Raman spectroscopy, TGA, and XRD demonstrated the high purity of the obtained material. The as-obtained FeS_2 was evaluated as a cathode material for lithium batteries and its lithiation/delithiation behavior was studied by means of galvanostatic charge/discharge cycles and electrochemical impedance spectroscopy. The resulting battery exhibited capacities of 470 mAh g^{-1} after 120 cycles, with Coulombic efficiencies close to 100%, making the obtained material a promising candidate for its application in large-scale production.

Experimental details

Materials

Iron powder (particle size < 10 μm, purity 99.9%), sulfur, polyvinylidenefluoride (PVdF), lithium bis(trifluoromethanesulfonyl)imide (LiTFSI), and tetraethylene glycol dimethyl ether (TEGDME) were purchased from Sigma-Aldrich. TIMCAL carbon superP was from MTI Technologies. Other reagents were battery grade and used without further purification.

Synthesis of FeS_2

The samples were prepared in an argon atmosphere using a planetary ball mill (Fritsch Pulverisette 7—Premium line). The precursor iron and sulfur powders, with a weight ratio of 0.33/0.67, were placed inside a hardened steel vial with balls of the same material. The balls-to-powder mass ratio was 10:1, and the rotation speed was set to 700 rpm. The powders were milled for 72 h. Small amounts of milled powder were taken at different times to control the synthesis. After the ball-milling, the powder was thermally treated at 350 °C for 1 h under vacuum to promote the full formation of the FeS_2 phase. The temperature for the thermal treatment was selected considering the minimum temperature needed to get the desired pure phase (the reader is referred to the Supporting Information for further details).

Characterization methods

The powder X-ray diffraction (XRD) patterns were recorded with a Philips PW1800/10 diffractometer using Cu-Kα radiation ($\lambda = 1.5405$ Å) in a 2θ range from 20° to 80°. The operation voltage and current were kept at 40 kV and 30 mA, respectively. Thermogravimetric analyses (TGA) of approximately 5 mg of each compound were recorded on a TGA Q600 (TA Instruments) under N_2 atmosphere, by equilibrating at 100 °C, and following a heating ramp rate of 10 °C min^{-1} up to 800 °C. The mean particle size of the powder and morphology was examined using a field emission scanning electron microscope (Zeiss Sigma FE-SEM) operating at 5 kV and a transmission electron microscope (Hitachi HT7700 high-resolution TEM) operating at 100 kV. Sample preparation for TEM images was done by dropping ethanol ultrasonicated suspensions of the synthetized material onto carbon-coated copper grids (400 mesh) and then dried. The Raman spectrum was measured in a Confocal Horiba Jobin-Yvon LabRam HR, using an excitation wavelength of 514.3 nm. The magnetic properties of the samples were determined with a vibrating-sample magnetometer (VSM, Lake Shore 7300). X-ray photoelectron spectroscopy (XPS) were collected using a Thermo Scientific™ K-Alpha™ + X-ray photoelectron spectrometer equipped with an Al-Kα radiation source (operating at 1200 W) and a hemispherical electrostatic electron energy analyzer. For the analysis, the C1s peak at 284.5 eV was used as reference to calibrate the binding-energy (BE) scale. The base pressure in the analysis chamber was 1×10^{-8} mbar. No degradation or changes in the spectra were observed during the experiments. ICP-OES determination was performed using a Shimadzu, ICPE-9820 instrument at PlaPiMu-LaSeISiC (UNLP-CIC) laboratory. The sample solution was prepared by an acid digestion method adding 15 mL HNO_3 and 5 mL of HCl to 0.1 g of powder. Then, 3 mL H_2O_2 was added and heated until all pyrite was dissolved. After that, the sample was cooled and the solution was diluted to 100 mL using tri-distilled water. The magnetization hysteresis loops were measured in a field ranging ± 13.5 kOe, at room temperature, with a Lakeshore 7300 vibrating sample magnetometer. Galvanostatic charge-discharge profiles and impedance spectroscopy (EIS) experiments were performed with an Arbin battery cycler (Arbin Instruments, USA) and an Autolab PGSTAT320N Potentiostat/Galvanostat (Metrohm, The Netherlands), respectively.

Electrode preparation and electrochemical measurements

The electrodes used for electrochemical measurements were prepared by doctor-blade coating a 9-μm-thick copper foil with a slurry made of FeS_2, TIMCAL carbon superP and PVdF binder (in a 3:6:1 mass proportion), using N-methyl-2-pyrrolidone as solvent. All the electrodes were dried at 80 °C for 2 h before introducing them in a glovebox (MBraun, filled with Ar atmosphere having less than 1 ppm concentration of O_2 and H_2O). The electrodes were punched into 12 mm diameter disks. The coin cells were assembled inside the glovebox using a Celgard 2325 membrane as separator with 40 μL electrolyte (1.0 M LiTFSI + 0.25 M $LiNO_3$ in TEGDME) and lithium foil as counter and reference electrode.

Results and discussion

Synthesis and characterization of FeS_2 nanoparticles

Fig. 1a shows the XRD patterns of the pure Fe and S powders used as precursors and of the mixture at different times of the milling. For an easier understanding of the structural evolution with milling time, the position of pyrite's main XRD peaks is indicated with dashed lines. After milling for 3 h, only the peaks of Fe and S are observed. After 24 h, new peaks appear indicating the formation of new phases coming from the reaction between iron and sulfur. In the XRD for the 72 h-milled mixture, FeS_2 broad peaks can be clearly seen along with others corresponding to Fe/S/Fe-S phases. Longer milling times do not change the peaks significantly. Since mechanical milling is not enough for promoting a complete reaction to pyrite, a thermal treatment at 350 °C in vacuum was performed. Figure 1b displays the diffractogram (normalized to the most intense peak) of the powder after the thermal treatment. It exhibits peaks at $2\theta = 28.3°$, 33.1°, 36.8°, 40.5°, 47.0°, 56.4°, 55.8°, 61.5°, and 64.2°, corresponding to the crystal planes (111), (200), (210), (211), (220), (311), (222), (320), and (321) of the cubic structure (PCPDF #96-901-001) indexed for pyrite (FeS_2). From the Rietveld analysis, single phase pyrite FeS_2, space group Pa3, is confirmed, with no segregation of secondary phases (within the detection limits of this technique). The lattice parameter obtained from the fit is 5.42471(6) Å and the crystallite size, calculated using the Williamson-Hall analysis considering all the reflection peaks, is 18 nm

The complete formation of FeS_2 after the thermal treatment was also confirmed by magnetic measurements (Fig. 2a). After milling for 72 h, the powder still has a relatively high magnetization, because of the presence of α-Fe, as previously determined by XRD. After the thermal treatment, a low magnetization is observed in good agreement with the expected behavior of the paramagnetic FeS_2 [43].

Thermogravimetric measurements in N_2 were also performed in order to fully characterize the obtained material (Fig. 2b). Before the thermal treatment, two weight loss

Fig. 1 a X-ray diffractograms of Fe, S and the mixture of the powders milled for 3 h, 24 h and 72 h. The dashed lines indicate the position of the main reflections coming from pyrite. b Rietveld refinement of the powder milled for 72 h after thermal treatment at 350 °C in vacuum
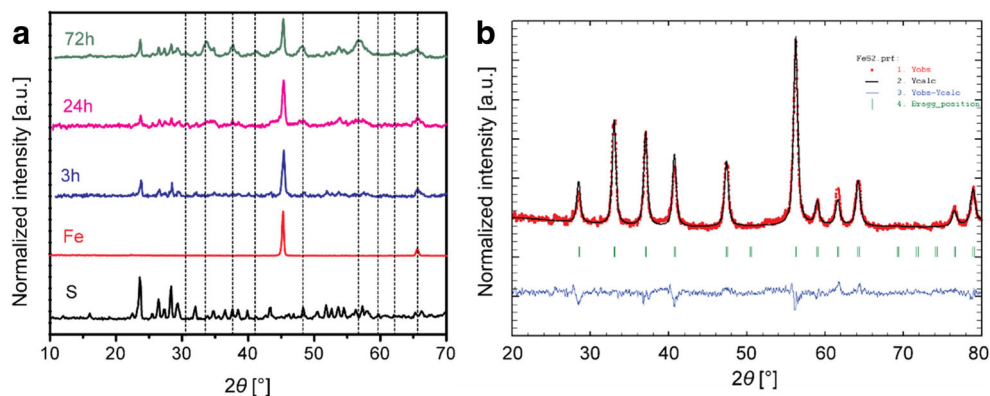

processes are observed, one at 300 °C corresponding to the free S evaporation and a second one at 600 °C corresponding to endothermic decomposition of pyrite to pyrrhotite [43]. After the thermal treatment, only one weight loss at 600 °C is observed, indicating the absence of S precursor in the sample. The weight loss of 20% is in perfect agreement with the theoretical mass change previously reported for the desulfurization of FeS_2 [15, 38]. Fe and S were titrated using ICP-OES measurements, where a Fe content of 440 mg/g of sample was found, indicating a S:Fe atomic ratio of 0.68:0.32 which is in good agreement with the pyrite composition.

The XPS spectra for S 2p and Fe 2p are shown in Fig. 3 a and b, respectively. The first two peaks of sulfur XPS spectrum at 162.4 and 163.6 eV BE correspond to the bulk S_2^{2-} $2p_{3/2}$ and $2p_{1/2}$ doublets of pyrite [54]. The little tail observed at low BE comes from the surface S_2^{2-} while the two peaks at 164.3 and 165.4 eV are a combination of core-hole effect signals and the presence, in the surface of the material, of oxidized S_n^{2-} species [13, 37]. The doublets at 168.6 and 169.82 eV correspond to the $2p_{3/2}$ and $2p_{1/2}$ SO_4^{2-} peaks, formed due to the surface oxidation of the sample. Fe^{2+} XPS peaks from FeS_2, in Fig. 3b, appear at 707.1 and 719.9 eV and correspond to the Fe $2p_{3/2}$ and $2p_{1/2}$ signals (iron exhibits a spin-orbit splitting of $\Delta_{metal} = 13$ eV). A small peak at 708.1 eV arises from the contribution of Fe^{2+} in electron deficient sites [41]. The

doublets at 709.1/721.6, 711.1/723.8, and the peak at 713.1 eV correspond to the $2p_{3/2}$ and $2p_{1/2}$ of FeO, $FeSO_4/Fe_2O_3$ and $Fe_2(SO_4)_3$ compounds (in the latter, the $2p_{1/2}$ peak is not seen because its expected intensity is in the order of the baseline noise) [37]. No Fe satellite peaks are observed as Fe^{2+} in pyrite is in low-spin configuration. The XPS spectra reveal that there is a surface oxidation of the material and therefore iron sulfates and iron oxides are in it, but the major component of the sample is pyrite. This is further corroborated by Raman spectroscopy, shown in Fig. 3c. The characteristic S_2 (E_g), S-S in-phase (A_g), and coupled vibration and stretch (T_g) modes of the pyrite are observed at 328, 363, and 412 cm^{-1}, respectively [2].

The morphology of the as-synthesized material was studied by SEM. Figure 4 shows the images at different magnifications. As can be seen, the sample consists of agglomerates of small particles of ~ 75 nm in diameter. The thermal treatment effect can be verified by comparing with the morphology of the untreated FeS_2 sample (depicted in Fig. S1), in which a deposit of sulfur can be seen on top of the pyrite aggregate. The TEM images of Fig. 5 display FeS_2 particles as disaggregated and having a spherical geometry with a Gaussian size distribution centered at 85 ± 2 nm mean diameter. The mean size obtained from TEM data is larger than the size of the crystallites calculated from the Williamson-Hall analysis, indicating that the particles are polycrystalline.

Fig. 2 a Magnetization hysteresis loops and b thermogravimetric measurements in N_2 atmosphere of the as-milled Fe and S mixture for 72 h and after the thermal treatment at 350 °C in vacuum
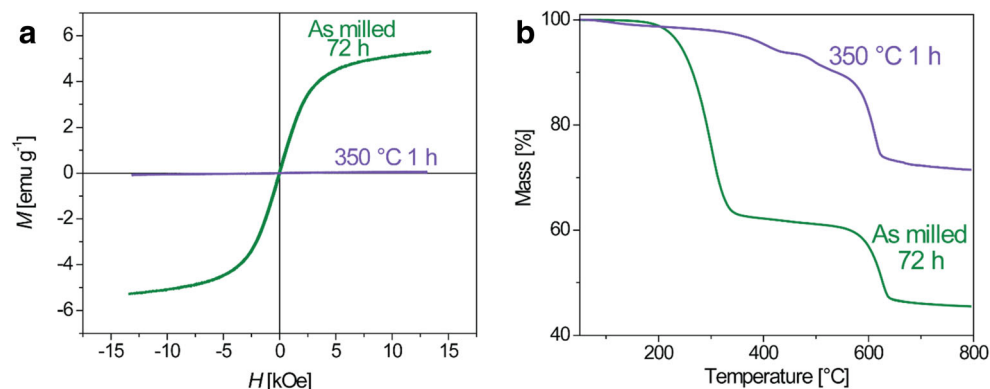
Fig. 3 Fitted XPS spectra for **a** S 2p and **b** Fe 2p of annealed pyrite. **c** Raman spectrum of the annealed FeS_2
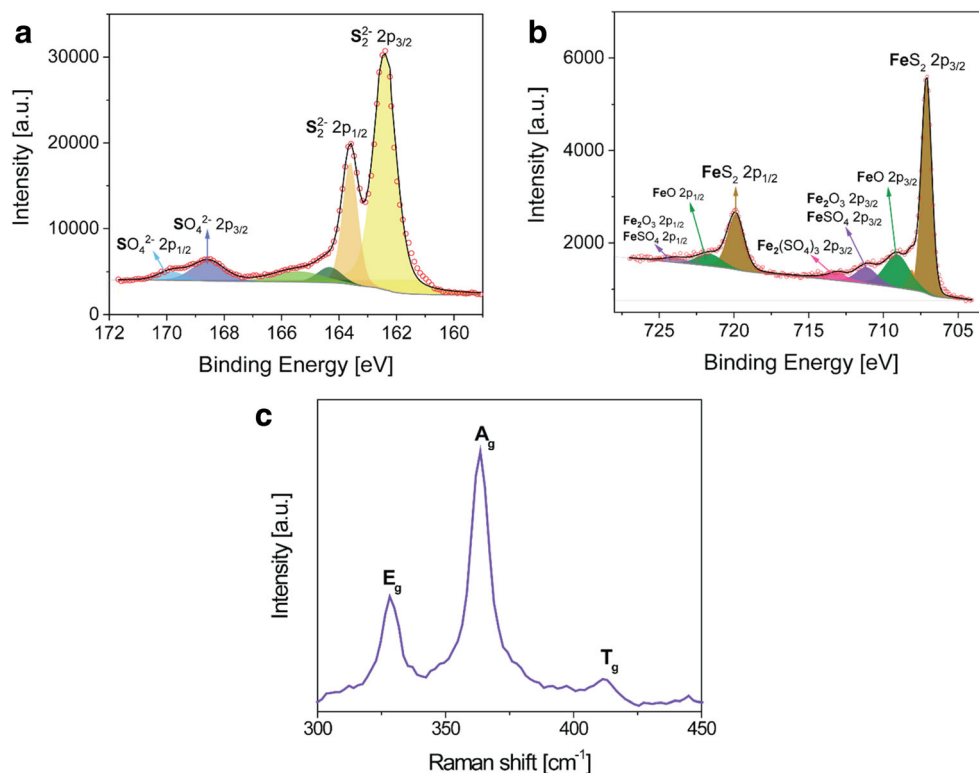

Electrochemical characterization and test as cathode for Li-batteries

The charge/discharge galvanostatic curves of the FeS_2 cathode for the first, second, and tenth cycle are displayed in Fig. 6a. The first discharge cycle shows a sloping voltage profile from 1.73 V until the experiment's cut-off limit, with an initial specific capacity of 1450 mAh g^{-1}. This high initial capacity is a frequently reported feature of Li/FeS_2 batteries [8, 18, 23, 39, 44, 47, 48] and could be related to the initial reduction of Fe-O oxides present in the material (as seen in the XPS spectra) and the SEI formation at the Li anode [46, 53] among others. It is worth mentioning that no phase change was observed in the active material after the processing of the slurry, as the XRD of the cathode shows no differences with the thermally treated pristine pyrite (Fig. S2). The dQ/dV curve for the first discharge cycle (Fig. 6b) shows multiple peaks associated with

a rather complex mechanism, which has been acknowledged as an irreversible reaction [33, 50, 52]. The subsequent charge cycle (black dashed curve in Fig. 6a) displays two voltage plateaus at ~1.84 and ~2.50 V, having this last one more capacity than the first. The features of the second discharge cycle are completely different from the first one due to the irreversible reaction, showing plateaus centered at ~2.00 V and ~1.47 V. As the cycling proceeds, the high-voltage plateaus are reduced and the capacity of the FeS_2 cathode fades.

FeS_2 can theoretically react with 4 Li^+ ions per formula unit, according to the global reaction given in Eq. 1 below, yielding a capacity of 894 mAh g^{-1} [10]. This first irreversible reaction occurs through a two-step mechanism in which there is first a breakage of S–S^{2-} bonds due to the formation of Li_2FeS_2 (Eq. 2), and then a conversion of Fe^{2+} to Fe^0 and the consequent release of Li_2S (Eq. 3). The probability of Eq. 1 going through one effective step or via Eqs. 2 and 3
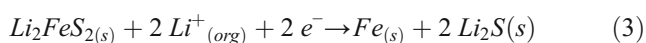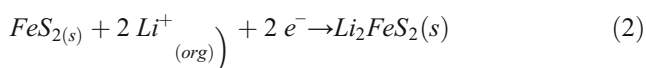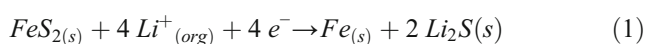
Fig. 4 SEM images of the thermally treated FeS_2 at two different magnifications
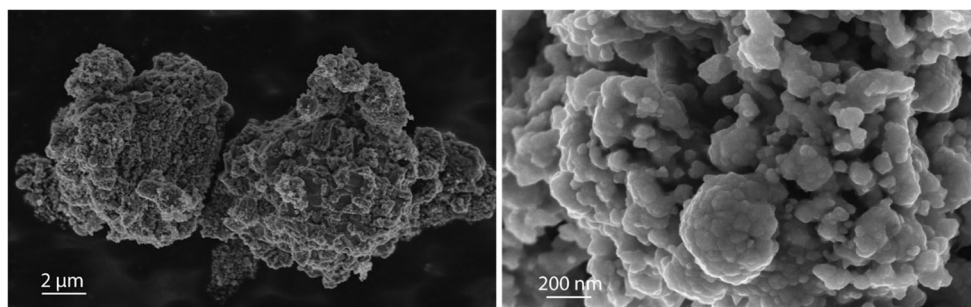
Fig. 5 TEM images of dispersed FeS$_2$ nanoparticles, at two different magnifications. Inset: size distribution determined over 100 nanoparticles
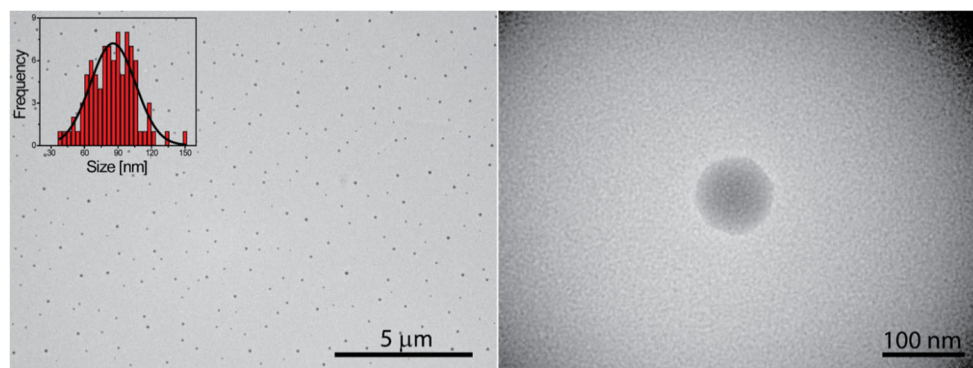
has been previously discussed and depends on the current/potential rate, temperature, and solvent [17, 31, 40].

$$FeS_{2(s)} + 4\,Li^+_{(org)} + 4\,e^- \rightarrow Fe_{(s)} + 2\,Li_2S(s) \quad (1)$$

$$FeS_{2(s)} + 2\,Li^+_{(org)}\big) + 2\,e^- \rightarrow Li_2FeS_2(s) \quad (2)$$

$$Li_2FeS_{2(s)} + 2\,Li^+_{(org)} + 2\,e^- \rightarrow Fe_{(s)} + 2\,Li_2S(s) \quad (3)$$

There is still controversy concerning FeS$_2$-based cathode subsequent charge/discharge reactions. Some reports suggest that Fe and Li$_2$S are recombined to form Li$_2$FeS$_2$/Li$_{2-x}$FeS$_2$ intermediates (lower voltage plateau), and ortho FeS$_2$ + FeS$_{8/7}$ + S structures (upper voltage plateau) [10, 17, 49]. Others postulate that the Fe/Li$_2$S oxidation mechanism follows two different pathways: first, delithiation of Li$_2$S + Fe forming a Fe$_x$S$_y$ phase (lower voltage plateau) and S/Li$_2$S known chemistry (upper voltage battery) [35, 36, 50, 51]. Regarding the latter, in our experiments, we did not find polysulfides either in the electrolyte or at the surface of the Li anode after cycling the Li-FeS$_2$ batteries. If the cycling would proceed through Li-S chemistry and taking into account that we are using TEGDME-based electrolyte, polysulfides should have been found due to their high solubility in the ether-based solvent [25]. In this work, instead of trying to fully identify possible intermediates and reduction/oxidation products, we will focus

our explanation on general trends and types of reactions that take place.

Cut-off 1 at the first dQ/dV peak of Fig. 6b (at 1.70 V, discharge/charge curves shown in Fig. S3 A) shows almost no plateau in the first recharge and the capacity fade between the first and the second cycle is 45%. Furthermore, cut-off 2 at the second dQ/dV peak of Fig. 6b (at 1.56 V, discharge/charge curves shown in Fig. S3 B) shows a capacity fade of 27%, demonstrating that the process associated to upper re-charge/discharge plateau is relatively independent of the lower one (at 1.84/1.47 V) in terms of features and capacity fading. Cut-off limited cycling up to the first plateau (Fig. S4) also showed the same behavior and capacity fading. Therefore, the electrochemical fingerprint of both processes after the first discharge is inherent to FeS$_2$ lithiation, and constrained cycling does not prevent its irreversible features and loss of capacity, contrary to what was suggested as a possible solution in previous reports [4, 35]. According to a recent thorough work by Butala et al. [1], the first recharge (and subsequent) plateau corresponds to the conversion of Fe and Li$_2$S to an intermediate ternary structure, while in the second one, this ternary Li-Fe-S phase acts as a host structure for insertion-extraction reaction with Li$^+$. The latter disappears rapidly both in our case and in other reported Li-FeS$_2$ systems: as this is an intercalation-deintercalation reaction, it

Fig. 6 a Charge-discharge galvanostatic curves for FeS$_2$ cathodes at 0.10 A g^{-1} for the first (black line), second (red line), and tenth (green line) cycle. b Derivative dQ/dV plots from the charge-discharge curves of panel a. The vertical lines in panel b labeled 1 and 2 correspond to the cut-off voltages used for the experiments in Fig. S3
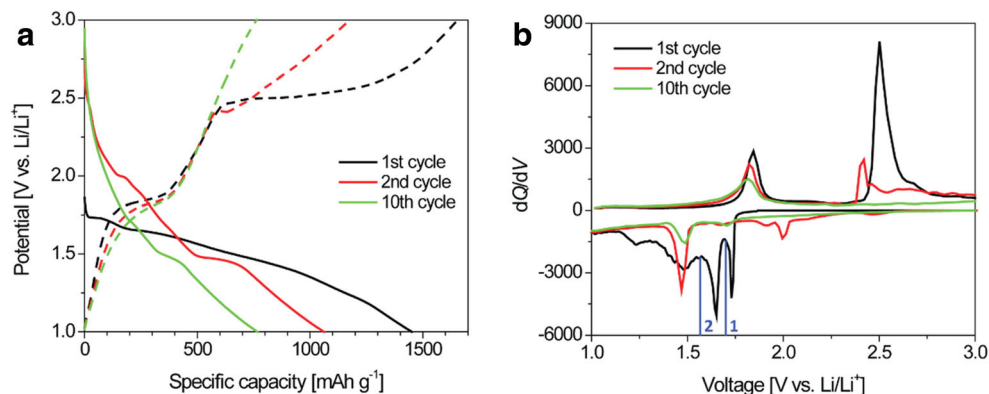
critically relies on the crystallinity of the host structure. As reported [1, 9], during cycling progressive amorphization of the phases is observed, so it is clear that this reaction will progressively fade.

EIS provides further information regarding the capacity fading. Figure 7a depicts the impedance spectra of FeS$_2$ cathodes at o.c.p. (blue circles in the inset), fully discharged (1.00 V, upper panel), and fully charged (3.00 V, bottom panel) for the first (black squares), second (red squares) and tenth (green squares) cycle. The impedance spectra were fitted with the equivalent circuit shown in Fig. S5. It consists of the solution/contact resistance (R_S) and the charge transfer resistance (R_{CT}) in parallel with a constant phase element (CPE) for the capacitive interfacial phenomena. These elements correspond to the high-frequency semi-circle, whose characteristic frequency varies from 924/2082 Hz to 763/1104 Hz for fully discharged/charged 1st and 10th cycle, respectively. In the mid-to-low frequency region, the features depend on if the fully charged (3.00 V) or discharged (1.00 V) state is under analysis. For the EI spectra at 1.00 V, a semicircular-like response can be noticed, with a characteristic frequency of 0.7–1 Hz, while at 3.00 V (and at o.c.p.) a linear dependence of -Z" vs Z' is observed, with one or two different slopes. For the latter, also the frequencies oscillate between 0.5 and 2 Hz. These frequency domains are associated with hindered Li$^+$ diffusion phenomena inside the porous electrode (limited mass transport) [6, 29], which correspond to the Z_{diff} element in the equivalent circuit of Fig. S5. The analysis of this behavior is beyond the aim of the present work, but it is a common feature observed in C-based composite electrodes and is frequently misinterpreted as an interfacial RC element. The effective capacitance of the process (C_{eff}) was calculated from the R_S, R_{CT}, and CPE elements according to previous theoretical framework [7, 14] and it is plotted as a function of the discharge/charge voltage, along with R_{CT}, in Fig. 7b (all the EI spectra corresponding to the intermediate potentials are depicted in Fig. S6).

Within any cycle, the resistances increase while discharging and decrease upon charging. As R_{CT} is inversely proportional to the concentration of active material, when lithiating, FeS$_2$ is consumed throughout the discharge so its amount diminishes, while the opposite holds when delithiating the cathode. Overall, when passing from the first to the second cycle, the capacitances are the values that decrease the most, especially from the first discharge to the first charge. This suggests that the main factor that contributes to capacity fading is the decrease in the total electroactive area. In this sense, detailed studies of phase transformations during lithiation of FeS$_2$ nanoparticles [9, 26] concluded that it proceeds via the radial movement of a reaction front into the particle, which consumes the pyrite and leaves behind intermixed Li$_2$S and Fe domains with a larger total volume. Upon recharging, a tri-phasic contact point must be
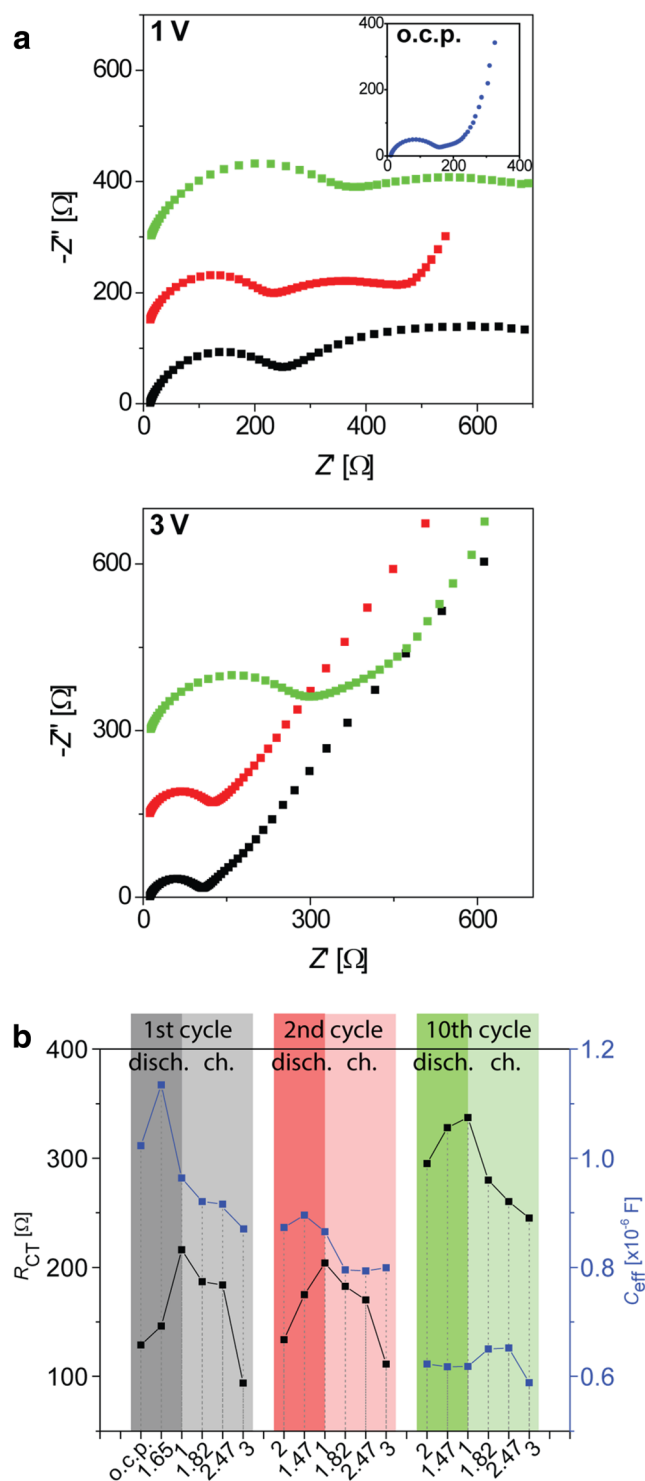
Fig. 7 a Impedance spectra of FeS$_2$ cathodes at o.c.p. (blue circles in the inset), discharged (1.00 V, upper panel) and charged (3.00 V, low panel) for the first (black squares), second (red squares), and tenth (green squares) cycle. EIS experimental conditions: $E_{dc} = 0.010$ V, frequency range = 10^5–10^{-2} Hz. b Charge transfer resistance (R_{CT}, left axis, black squares) and effective capacitance (C_{eff}, right axis, blue squares) obtained from the EIS of panel a, as a function of the potential of discharge/charge galvanostatic cycling. For a better interpretation of the graphics, the values corresponding to each cycle have been depicted using the same color scheme as that employed in panel a

Fig. 8 a Cycling performance of the FeS$_2$ cathode at 0.10 A g^{-1} for the discharge (red circles) and charge (black circles) processes. The right axis shows the Coulombic efficiency. b Rate capability of the FeS$_2$ cathode at various current densities
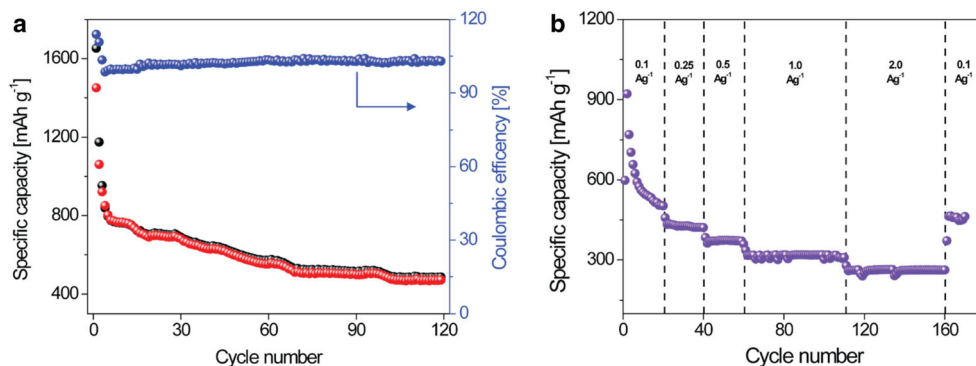
established between Li$_2$S, Fe, and Li$^+$ in the electrolyte for the reaction to take place. Therefore, the change in the volume and phase segregation reduces the surface of contact in which these three phases meet to react. Concomitantly, after 10 cycles, important changes are also observed in R_{CT}, which increases notably compared to the previous cycles. In this case, the main cause for the capacity fading is the sluggishness of the electrochemical processes because of the loss of active material.

As a final remark, we would like to point out that the specific capacities are calculated based on the initial irreversible reaction of FeS$_2$ and subsequent battery operation occurs by a still not fully understood mechanism. Therefore, "capacity fading" in Li/FeS$_2$ is a phenomenon that should be revisited in the future with a complete characterization of the intervening species, to allow the assessment of the full reaction mechanism without doubts.

In spite of the above-discussed issues with pyrite's electrochemical mechanism and capacity fading, the present cathode exhibits a competitive specific capacity. Figure 8 displays the cyclability of Li-FeS$_2$ battery for 120 discharge/charge cycles (a) and the rate capability for 180 cycles at various current densities (b). This cathode delivered a specific capacity of 470 mAh g^{-1} after 120 cycles and showed capacities as high as 300 mAh g^{-1} even at current densities of 2.00 A g^{-1}. After high C rate cycling and when returning to the initial 0.10 A g^{-1} current density value, a retention of 92% of capacity is

observed. The obtained results confirm the excellent electrochemical behavior of the material resulting from an inexpensive and simple method for developing potential cathodes for lithium batteries.

Furthermore, a brief comparison with other FeS$_2$ cathodes proposed in the literature (presented in Table 1) shows that that the present cathode material is very competitive in terms of specific capacity value and cyclability. The comparison presented here includes only equivalent systems that use pristine FeS$_2$ as active cathode material, without considering its composites with carbon materials or other oxides. It has been postulated that the use of composite materials should boost capacity retention due to the presence of different phases able to be lithiated and the possibility of buffering FeS$_2$ structural changes during lithiation/delithiation [3, 34]. Nonetheless, and to the best of our knowledge, in most reported publications, a strong capacity fading is also observed, typical of conversion-type cathodes [45].

Conclusions

Pyrite was obtained via a scalable and low-cost mechanochemical synthetic route, followed by a thermal treatment. The obtained FeS$_2$ powder was single phase and consisted of spherical particles with a mean particle size of 85 nm and crystallite size of 18 nm. The as-prepared pyrite was tested as

Table 1 Comparative analysis of cathodes prepared using FeS$_2$ as active material for lithium batteries

Active material*	Initial specific capacity [mAh g^{-1}]	Current density	Specific capacity after cycling (number of cycles) [mAh g^{-1}]	Ref.
FeS$_2$ nanoparticles	574.6	0.2 mA cm^{-2}	332 (2)	[42]
FeS$_2$—porous microsphere	425	0.10 A g^{-1}	216.8 (730)	[24]
FeS$_2$	849	0.2 mA cm^{-2}	492 (50)	[35]
FeS$_2$	~800	0.2 C	250 (70)	[34]
FeS$_2$	~230	0.5 C	76.9 (200)	[3]
FeS$_2$ microsphere	842	0.1 A g^{-1}	683 (10)	[16]
FeS$_2$	740	0.5 C	185 (50)	[22]
FeS$_2$ nanoparticles	1450	0.1 A g^{-1}	470 (120)	Our work

an active material for cathodes in lithium batteries. The material presents a high specific capacity of 470 mAh g^{-1} after 120 cycles, without memory effects after working with current densities as high as 2.00 A g^{-1}. The simplicity of preparation and the high cyclability, make the proposed synthetic route promising for practical applications in real technological processes. Our work also points out the need of carrying on a deeper study about the electrochemistry behind the mechanisms that take place when using pyrite as a cathode material, in order to have a better understanding of the capacity fading issues of these cathodes.

References

1. Butala MM, Mayo M, Doan-Nguyen VVT, Lumley MA, Göbel C, Wiaderek KM, Borkiewicz OJ, Chapman KW, Chupas PJ, Balasubramanian M, Laurita G, Britto S, Morris AJ, Grey CP, Seshadri R (2017) Local structure evolution and modes of charge storage in secondary Li–FeS$_2$ cells. Chem Mater 29(7):3070–3082

2. Chen M, Liu X, Qi M, Xiang J, Yin J, Chen Q, Xia X (2017) Tailored integrated electrodes of graphene foam supported FeS$_2$ as cathode for enhanced Li ion storage performance. Mater Technol 32:888–892

3. Chen W, Qi S, Yu M, Feng X, Cui S, Zhang J, Mi L (2017) Design of FeS$_2$@rGO composite with enhanced rate and cyclic performances for sodium ion batteries. Electrochim Acta 230:1–9

4. Cheng S, Wang J, Lin H, Li W, Qiu Y, Zheng Z, Zhao X, Zhang Y (2017) Improved cycling stability of the capping agent-free nanocrystalline FeS$_2$ cathode via an upper cut-off voltage control. J Mater Sci 52(5):2442–2451

5. Choi S, Wang G (2018) Advanced Lithium-ion batteries for practical applications: technology, development, and future perspectives. Adv Mater Technol 3(9):1700376

6. Cooper SJ, Bertei A, Finegan DP, Brandon NP (2017) Simulated impedance of diffusion in porous media. Electrochim Acta 251: 681–689

7. Córdoba-Torres P, Mesquita TJ, Nogueira RP (2015) Relationship between the origin of constant-phase element behavior in electrochemical impedance spectroscopy and electrode surface structure. J Phys Chem C 119(8):4136–4147

8. Ding X, Du C, Li J, Huang X (2019) FeS$_2$ microspheres wrapped by N-doped rGO from an Fe-based ionic liquid precursor for rechargeable lithium ion batteries. Sustain Energy Fuels 3(3):701–708

9. Douglas A, Carter R, Oakes L, Share K, Cohn AP, Pint CL (2015) Ultrafine iron pyrite (FeS$_2$) nanocrystals improve sodium–sulfur and lithium–sulfur conversion reactions for efficient batteries. ACS Nano 9(11):11156–11165

10. Fong R, Dahn JR, Jones CHW (1989) Electrochemistry of pyrite-based cathodes for ambient temperature lithium batteries. J Electrochem Soc 136(11):3206–3210

11. Golodnitsky D, Peled E (1999) Pyrite as cathode insertion material in rechargeable lithium/composite polymer electrolyte batteries. Electrochim Acta 45(1-2):335–350

12. Grayfer ED, Pazhetnov EM, Kozlova MN, Artemkina SB, Fedorov VE (2017) Anionic redox chemistry in polysulfide electrode materials for rechargeable batteries. ChemSusChem 10(24):4805–4811

13. Herbert FW, Krishnamoorthy A, Ma W, Van Vliet KJ, Yildiz B (2014) Dynamics of point defect formation, clustering and pit initiation on the pyrite surface. Electrochim Acta 127:416–426

14. Hirschorn B, Orazem ME, Tribollet B, Vivier V, Frateur I, Musiani M (2010) Determination of effective capacitance and film thickness from constant-phase-element parameters. Electrochim Acta 55(21): 6218–6227

15. Hong Y, Fegley B (1997) The kinetics and mechanism of pyrite thermal decomposition. Berichte der Bunsengesellschaft für Phys Chemie 101(12):1870–1881

16. Hu Z, Zhang K, Zhu Z, Tao Z, Chen J (2015) FeS$_2$ microspheres with an ether-based electrolyte for high-performance rechargeable lithium batteries. J Mater Chem A 3(24):12898–12904

17. Jones CHW, Kovacs PE, Sharma RD, McMillan RS (1991) An iron-57 Moessbauer study of the intermediates formed in the reduction of iron disulfide in the lithium/iron disulfide battery system. J Phys Chem 95(2):774–779

18. Al Khateeb S, Sparks TD (2019) Spray pyrolysis of conductor- and binder-free porous FeS$_2$ films for high-performance lithium ion batteries. J Mater Sci 54(5):4089–4104

19. Kim TH, Kim SG (2011) Clinical outcomes of occupational exposure to N,N-dimethylformamide: perspectives from experimental toxicology. Saf Health Work 2(2):97–104

20. Li L, Caban-Acevedo M, Girard SN, Jin S (2014) High-purity iron pyrite (FeS$_2$) nanowires as high-capacity nanostructured cathodes for lithium-ion batteries. Nanoscale 6(4):2112–2118

21. Li M, Lu J, Chen Z, Amine K (2018) 30 years of lithium-ion batteries. Adv Mater 30(33):1800561

22. Liu J, Wen Y, Wang Y, Van Aken PA, Maier J, Yu Y (2014) Carbon-encapsulated pyrite as stable and earth-abundant high energy cathode material for rechargeable lithium batteries. Adv Mater 26(34): 6025–6030

23. Liu WL, Rui XH, Tan HT, Xu C, Yan QY, Hng HH (2014) Solvothermal synthesis of pyrite FeS$_2$ nanocubes and their superior high rate lithium storage properties. RSC Adv 4(90):48770–48776

24. Ma W, Liu X, Lei X, Yuan Z, Ding Y (2018) Micro/nano-structured FeS$_2$ for high energy efficiency rechargeable Li-FeS$_2$ battery. Chem Eng J 334:725–731

25. Markevich E, Salitra G, Talyosef Y, Chesneau F, Aurbach D (2017) Review—on the mechanism of quasi-solid-state lithiation of sulfur encapsulated in microporous carbons: is the existence of small sulfur molecules necessary? J Electrochem Soc 164(1):A6244–A6253

26. McDowell MT, Lu Z, Koski KJ, Yu JH, Zheng G, Cui Y (2015) In situ observation of divergent phase transformations in individual sulfide nanocrystals. Nano Lett 15(2):1264–1271

27. Pan GX, Cao F, Xia XH, Zhang YJ (2016) Exploring hierarchical FeS$_2$/C composite nanotubes arrays as advanced cathode for lithium ion batteries. J Power Sources 332:383–388

28. Pearce CI (2006) Electrical and magnetic properties of sulfides. Rev Mineral Geochem 61(1):127–180

29. Radvanyi E, Porcher W, De Vito E, Montani A, Franger S, Jouanneau Si Larbi S (2014) Failure mechanisms of nano-silicon anodes upon cycling: an electrode porosity evolution model. Phys Chem Chem Phys 16(32):17142–17153

30. Shao-Horn Y, Horn QC (2001) Chemical, structural and electrochemical comparison of natural and synthetic FeS$_2$ pyrite in lithium cells. Electrochim Acta 46(17):2613–2621

31. Shao-Horn Y, Osmialowski S, Horn QC (2002) Reinvestigation of lithium reaction mechanisms in FeS$_2$ pyrite at ambient temperature. J Electrochem Soc 149(12):A1547–A1555

32. Son SB, Yersak TA, Piper DM, Kim SC, Kang CS, Cho JS, Suh SS, Kim YU, Oh KH, Lee SH (2014) A stabilized PAN-FeS$_2$ cathode with an EC/DEC liquid electrolyte. Adv Energy Mater 4:2–6

33. Strauss E, Golodnitsky D, Peled E (2002) Elucidation of the charge-discharge mechanism of lithium/polymer electrolyte/pyrite batteries. J Solid State Electrochem 6(7):468–474

34. Su Q, Lu Y, Liu S, Zhang X, Lin Y, Fu R, Wu D (2018) Nanonetwork-structured yolk-shell FeS$_2$@C as high-performance cathode materials for Li-ion batteries. Carbon 140:433–440

35. Sun K, Cama CA, DeMayo RA, Bock DC, Tong X, Su D, Marschilok AC, Takeuchi KJ, Takeuchi ES, Gan H (2017) Interaction of FeS$_2$ and sulfur in Li-S battery system. J Electrochem Soc 164(1):A6039–A6046

36. Sun K, Wu Q, Gan H (2018) Molecular insights into ether-based electrolytes for Li-FeS$_2$ batteries. Energy Storage Mater 12:85–93

37. Tauson VL, Babkin DN, Lustenberg EE, Lipko SV, Parkhomenko IY (2008) Surface typochemistry of hydrothermal pyrite: electron spectroscopic and scanning probe microscopic data. I. Synthetic pyrite. Geochem Int 46(6):565–577

38. Thomas PS, Hirschausen D, White RE, Guerbois JP, Ray AS (2003) Characterisation of the oxidation products of pyrite by thermogravimetric and evolved gas analysis. J Therm Anal Calorim 72:769–776

39. Tran DT, Dong H, Walck SD, Zhang SS (2015) Pyrite FeS$_2$–C composite as a high capacity cathode material of rechargeable lithium batteries. RSC Adv 5(107):87847–87854

40. Tryk DA, Kim S, Hu Y, Xing W, Scherson DA, Antonio MR, Leger VZ, Blomgren GE (1995) Electrochemical insertion of lithium into pyrite from nonaqueous electrolytes at room temperature: an in situ Fe K-edge X-ray absorption fine structure study. J Phys Chem 99(11):3732–3735

41. Uhlig I, Szargan R, Nesbitt HW, Laajalehto K (2001) Surface states and reactivity of pyrite and marcasite. Appl Surf Sci 179(1-4):222–229

42. Wang S, Yu J (2016) Electrochemical mechanism for FeS$_2$/C composite in lithium ion batteries with enhanced reversible capacity. Energies 9(4):225

43. Waters KE, Rowson NA, Greenwood RW, Williams AJ (2008) The effect of heat treatment on the magnetic properties of pyrite. Miner Eng 21(9):679–682

44. Wen X, Wei X, Yang L, Shen PK (2015) Self-assembled FeS$_2$ cubes anchored on reduced graphene oxide as an anode material for lithium ion batteries. J Mater Chem A 3(5):2090–2096

45. Wu F, Yushin G (2017) Conversion cathodes for rechargeable lithium and lithium-ion batteries. Energy Environ Sci 10(2):435–459

46. Xiong S, Xie K, Diao Y, Hong X (2014) Characterization of the solid electrolyte interphase on lithium anode for preventing the shuttle mechanism in lithium–sulfur batteries. J Power Sources 246:840–845

47. Xu Q-T, Xue H-G, Guo S-P (2018) FeS$_2$ walnut-like microspheres wrapped with rGO as anode material for high-capacity and long-cycle lithium-ion batteries. Electrochim Acta 292:1–9

48. Xu X, Cai T, Meng Z, Ying H, Xie Y, Zhu X, Han WQ (2016) FeS$_2$ nanocrystals prepared in hierarchical porous carbon for lithium-ion battery. J Power Sources 331:366–372

49. Yersak TA, Macpherson HA, Kim SC, Le V-D, Kang CS, Son S-B, Kim Y-H, Trevey JE, Oh KH, Stoldt C, Lee S-H (2012) Solid state enabled reversible four electron storage. Adv Energy Mater 3:120–127

50. Zhang SS (2015) The redox mechanism of FeS$_2$ in non-aqueous electrolytes for lithium and sodium batteries. J Mater Chem A 3(15):7689–7694

51. Zhang SS, Tran DT (2015) Electrochemical verification of the redox mechanism of FeS$_2$ in a rechargeable lithium battery. Electrochim Acta 176:784–789

52. Zhang SS, Tran DT (2016) Mechanism and solution for the capacity fading of Li/FeS$_2$ battery. J Electrochem Soc 163(5):A792–A797

53. Zhang X-Q, Cheng X-B, Zhang Q (2018) Advances in interfaces between Li metal anode and electrolyte. Adv Mater Interfaces 5(2):1701097

54. Zhu J, Xian H, Lin X, Tang H, Du R, Yang Y, Zhu R, Liang X, Wei J, Teng HH, He H (2018) Surface structure-dependent pyrite oxidation in relatively dry and moist air: implications for the reaction mechanism and sulfur evolution. Geochim Cosmochim Acta 228:259–274

55. Energizer® Ultimate Lithium™ AA battery. http://www.energizer.com/batteries/energizer-ultimate-lithium-batteries. Accessed 9 May 2019